Flight Simulation and Control of a Helicopter Undergoing Rotor Chord Extension Morphing

Jayanth Krishnamurthi
Graduate Research Assistant
Rensselaer Polytechnic Institute
Troy, NY 12180

Farhan Gandhi
Redfern Professor of Aerospace Engineering
Rensselaer Polytechnic Institute
Troy, NY 12180

ABSTRACT

The current study focuses on flight simulation and control of a helicopter undergoing rotor chord morphing. A model-following dynamic inversion controller with inner and outer loop control laws (CLAWS) is implemented and chord extension is introduced as an additional feedforward component to the inner loop CLAW. Simulation results based on a chord-morphing variant of the UH-60A Black Hawk helicopter at 20,000 lbs gross weight are presented. From the baseline rotor blade, the chord is increased from 63% to 83% of the rotor span by means of a trailing-edge plate (TEP) extension at a deployment angle of 2 degrees. Chord morphing at sea-level and hot-and-high conditions are considered. The controller is shown to regulate the operating state of the aircraft well over the nominal morphing duration of 60 seconds and also for reduced durations down to 15 seconds. Differences between baseline and morphed states are discussed. In addition, the performance of the controller with respect to rate of morphing is evaluated and the effect of asynchronous morphing is also considered.

NOTATION

A	System matrix
B	Control matrix
c	Elemental blade chord (ft)
C	Output matrix
C_l, C_d	Elemental lift, drag, and moment coefficients
C_m	
dL, dD	Elemental lift, drag, and moment (lbs)
dM	
dr	Length of blade element (ft)
D	Direct feedthrough matrix
e	Error vector
g	Gravitational acceleration (ft/s^2)
K_C	Collective feedforward gain
K_D	Derivative gain
K_I	Integral gain
K_P	Proportional gain
p, q, r	Body-frame rotational velocities (rad/s)
Q_e	Engine torque (ft-lbs)
$\vec{u}$	Control vector
u, v, w	Body-frame translational velocities (ft/s)
U_∞	Elemental free-stream velocity (ft/s)
V_X, V_Y	Inertial velocities (ft/s)
V_Z	
$\vec{x}$	State vector
$\vec{y}$	Output vector
X, Y, Z	Inertial positions (ft)
X_u, X_v	Speed stability derivatives (1/s)
Y_u, Y_v	
β	Rotor flapping angle (rad)
δ	Control input (%)
$\Delta()$	Change in quantity
ε	Trailing-edge-plate extension (%)
ζ	Damping ratio
η	TEP deployment angle (deg)
θ	Pitch attitude (rad)
λ	Inflow ratio
ν	Pseudo-command
ρ	Air density (slugs/ft^3)
τ	Time constant (sec)
ϕ	Roll attitude (rad)
χ_f	Engine fuel flow (lbm/s)
ψ	Yaw attitude (rad)
ω_n	Natural frequency (rad/s)
Ω	Rotor rotational speed (rad/s)
$()_{lat}$	Lateral input/component
$()_{1s}$	
$()_{long}$	Longitudinal input/component
$()_{1c}$	
$()_{coll}$	Collective input/component
$()_0$	
$()_{ped}$	Pedal input/component
$()_{0_{TR}}$	
$()_{tht}$	Throttle input
$()_d$	Differential component
$()_1$	Primary control inputs/components
$()_2$	Morphing control inputs/components

Presented at the AHS 72nd Annual Forum, West Palm Beach, Florida, May 17–19, 2016.

$()_r$	Reduced-order
$()_{cmd}$	Commanded value
$()_{ref}$	Reference value
$()_{inner}$	Pertaining to the inner loop CLAW
$()_{outer}$	Pertaining to the outer loop CLAW

INTRODUCTION

With the optimum rotor geometry known to vary depending on the operating state, a fixed-geometry rotor can perform optimally in a specific set of conditions with significant penalties in other conditions, or alternatively, represent a compromise design with adequate but sub-optimal performance in most conditions. Recently, there has been significant interest in rotor morphing, or reconfiguration, to enhance performance in diverse operating conditions, as well as expand the flight envelope and operational flexibility of rotary-wing aircraft. Although rotor morphing faces substantially greater challenges than morphing in fixed-wing aircraft due to a smaller available area in which to fit the actuators and morphing mechanisms, requirement for these to operate in the presence of a large centrifugal field, and requirement for power transfer to the rotating system, the potential pay-off is even greater. Among the various methods of rotor morphing considered in the literature, rotor chord extension morphing (Refs. 1–5) is advantageous when the aircraft is operating in stall-dominant conditions. In Ref. 2, it was shown that for a UH-60A Black Hawk Helicopter, chord extension could reduce rotor power requirements by as much as 18% at high gross weight and altitude. The study also showed increases of 18 knots in maximum speed capability, 1500 lbs. in maximum gross-weight capability, and 1800 ft. in maximum altitude, with chord extension. The ability to selectively extend the rotor blade chord in stall-dominant conditions is advantageous over using fixed-geometry, wide-chord rotor blades as the latter results in undesirable profile drag penalties at moderate operating conditions (where the aircraft is not near the envelope boundary and susceptible to stall). A number of different rotor chord extension mechanisms have been considered in the literature to demonstrate feasibility of the concept, as seen, for example, in Refs. 3–5. The studies described on rotor chord morphing have thus far focused broadly on quantifying potential performance benefits and possible implementation methods. However, transient behavior and control of the aircraft during the chord morphing process has thus far received no attention. A helicopter undergoing chord morphing will naturally tend to leave its trimmed flight condition. In order for the aircraft to maintain its current operating condition (speed, altitude, heading etc.), compensatory primary control inputs would be required. Recently, Ref. 6 addressed this gap in knowledge for rotor span morphing. That study focused on the design and application of a model-following dynamic inversion controller to maintain the aircraft's current operating state during rotor span morphing. The current study follows Ref. 6 and focuses on application of the controller for rotor chord morphing. Simulation results are provided for a UH-60A Black Hawk helicopter in forward flight to demonstrate the effectiveness of the controller during morphing, and the differences between the baseline and morphed states are discussed as well. The controller's effectiveness is also considered with respect to rate of morphing and asynchronous morphing.

SIMULATION MODEL

A simulation model of the UH-60A Black Hawk has been developed in-house, which is a derivative of Sikorsky's GenHel model (Ref. 7). The model includes a non-linear, blade element representation of a single main rotor with articulated blades using airfoil table look-up. The blades themselves are approximated to be rigid, undergoing rotations about an offset flapping hinge. The lag degree of freedom is neglected. The 3-state Pitt-Peters dynamic inflow model (Ref. 8) is used to represent the induced velocity distribution on the rotor disk. The tail rotor forces and torque are based on the closed-form Bailey rotor model (Ref. 9), with the inflow distribution calculated using the uniform component of the Pitt-Peters model. The rigid fuselage and empennage (horizontal and vertical tail) forces and moments are implemented as look-up tables based on wind tunnel data from the GenHel model. A simple 3-state generic engine model given by Padfield (Ref. 10) is used for the propulsion dynamics, with the governing time constants approximated based on the GenHel engine model.

$$\begin{aligned} \dot{\vec{x}} &= f(\vec{x}, \vec{u}) \\ \vec{y} &= g(\vec{x}, \vec{u}) \end{aligned} \tag{1}$$

where $\vec{y}$ is a generic output vector. The state vector, $\vec{x}$, is given by

$$\begin{aligned} \vec{x} = [&u, v, w, p, q, r, \phi, \theta, \psi, X, Y, Z, \\ &\beta_0, \beta_{1s}, \beta_{1c}, \beta_d, \dot{\beta}_0, \dot{\beta}_{1s}, \dot{\beta}_{1c}, \dot{\beta}_d, \lambda_0, \lambda_{1s}, \lambda_{1c}, \lambda_{0_{TR}} \\ &\Omega, \chi_f, Q_e]^T \end{aligned} \tag{2}$$

The state vector comprises of 12 fuselage states (3 body velocities (u,v,w), 3 rotational rates (p,q,r), 3 attitudes (ϕ,θ,ψ), and 3 inertial positions (X,Y,Z), 11 rotor states (4 blade flapping states $(\beta_0,\beta_{1s},\beta_{1c},\beta_d)$ and their derivatives in multi-blade coordinates, and 3 rotor inflow states $(\lambda_0,\lambda_{1s},\lambda_{1c})$), tail rotor inflow state $(\lambda_{0_{TR}})$, and 3 propulsion states (rotational speed (Ω), engine fuel flow (χ_f) and engine torque (Q_e). The control input vector is given by

$$\vec{u} = \left[\delta_{lat}, \delta_{long}, \delta_{coll}, \delta_{ped}, \delta_{thl}\right]^T \tag{3}$$

and is comprised of lateral, longitudinal, and collective stick inputs to the main rotor, pedal input to the tail rotor, and throttle input to the engine.

Baseline Model Validation

The baseline simulation model was validated against a trim sweep of flight test and GenHel data (Ref. 11), for a gross weight of 16000 lbs and altitude of 5250 ft. For validation purposes alone, elastic twist deformations on the blades, based on an empirical correction in the GenHel model (Ref. 7), were incorporated to improve the correlation of the simulation model. Figure 1 shows representative results and the baseline simulation model correlates well with both flight test and GenHel. For the design of control laws, the nonlinear equations of motion were linearized using numerical perturbation at specific operating conditions. The linearized version of Equation 1 can be written as

$$\begin{aligned} \Delta\dot{\vec{x}} &= A\Delta\vec{x} + B\Delta\vec{u} \\ \Delta\vec{y} &= C\Delta\vec{x} + D\Delta\vec{u} \end{aligned} \tag{4}$$

Validation of the linear model with GenHel and flight data (Ref. 12) is shown in Figure 2 for hover and 80 knots forward flight, for a gross weight of 15350 lbs at sea level. The model correlates fairly well in the frequency range of 0.5-10 rad/s, as shown.

Variable Chord Rotor Blade

The simulation model is now modified to incorporate chord morphing on the blades, based on prior work reported in Refs. 2, 13. A schematic of the mechanism is illustrated in Figure 3, taken from Ref.2. As shown in the figure, chord extension is achieved by means of an extendable trailing-edge plate (TEP), where the length of extension, ε, is given as a percent of the nominal airfoil chord and the angle of deflection, η, is measured relative to the chord line. The chord extension is implemented between 63% and 83% span on the UH-60A blade. Refs. 2 and 13 point out that the extension of the TEP alters the sectional aerodynamic coefficients through the increased chord length and the change in the resulting airfoil profile. The sectional aerodynamic coefficients (C_l, C_d, C_m) utilized in this study are normalized with respect to the extended chord. Figure 4 shows the lift and moment coefficients of the baseline SC-1094R8 airfoil and modified versions incorporating a TEP extension of $\varepsilon = 20\%$ and deflection angles of $\eta = 0$, $\eta = 2$, and $\eta = 4$ degrees for Mach 0.4. They are derived using a Navier-Stokes computational fluid dynamics (CFD) code and presented in more detail in Ref. 13. In this study, a deflection angle of $\eta = 2$ degrees is used throughout the simulations (see section on results). The elemental lift, drag, and moment are then given by

$$\begin{aligned} dL &= \frac{1}{2}\rho U_\infty^2 (c+\varepsilon) C_l dr \\ dD &= \frac{1}{2}\rho U_\infty^2 (c+\varepsilon) C_d dr \\ dM &= \frac{1}{2}\rho U_\infty^2 (c+\varepsilon)^2 C_m dr \end{aligned} \tag{5}$$

where ρ, and U_∞ are the density and elemental free stream velocity. With this modified blade, an additional chord morphing input is specifically introduced into the dynamics given by Equation 1. The equations of motion now become

$$\begin{aligned} \dot{\vec{x}} &= f\left(\vec{x}, \vec{u}_1, \vec{u}_2\right) \\ \vec{y} &= g\left(\vec{x}, \vec{u}_1, \vec{u}_2\right) \end{aligned} \tag{6}$$

where u_1 is now the primary input vector given by Equation 3 and u_2 is the morphing input vector given by

$$\vec{u}_2 = \varepsilon \tag{7}$$

Correspondingly, the linear model for the baseline aircraft given by Equation 4 now becomes

$$\begin{aligned} \Delta\dot{\vec{x}} &= A\Delta\vec{x} + B_1\Delta\vec{u}_1 + B_2\Delta\vec{u}_2 \\ \Delta\vec{y} &= C\Delta\vec{x} + D_1\Delta\vec{u}_1 + D_2\Delta\vec{u}_2 \end{aligned} \tag{8}$$

where B_1 and B_2 are the control matrices that correspond to the primary and morphing input vectors, respectively.

CONTROL SYSTEM DESIGN

The design of the control system is based on model following linear dynamic inversion (DI) (Ref. 14). Model following concepts are widely used in modern rotorcraft control systems for their ability to achieve task-tailored handling qualities via independently setting feed-forward and feedback characteristics (Ref. 15). In addition, the dynamic inversion controller typically does not require gain scheduling since it takes into account the nonlinearities of the aircraft (i.e. a model of the aircraft is built into the controller). It is thus suitable for a wide range of flight conditions (Ref. 14).

A schematic of the overall control system is shown in Figure 5. The control system is effectively split into inner and outer loop control laws (CLAWS). In designing the CLAWS, the full 26-state linear model given by Equation 8 was reduced to an 8-state quasi-steady model. Firstly, the rotor RPM degree of freedom (Ω) is assumed to be regulated via the throttle input determined by the RPM Governor, with the remaining propulsion states (χ_f and Q_e) coupling only with Ω. Therefore, the propulsion states and throttle input are truncated from the linear

model. Secondly, since the rotor dynamics are considerably faster than the fuselage dynamics, they can essentially be considered as quasi-steady states and folded into the fuselage dynamics (Ref. 10), which reduces computational cost. The resulting system is an effective 8-state quasi-steady model whose state and control vectors are given by

$$\begin{aligned} \Delta\vec{x}_r &= [\Delta u, \Delta v, \Delta w, \Delta p\, \Delta q, \Delta r, \Delta\phi, \Delta\theta]^T \\ \Delta\vec{u}_{1r} &= \left[\Delta(\delta_{lat}), \Delta\left(\delta_{long}\right), \Delta(\delta_{coll}), \Delta\left(\delta_{ped}\right)\right]^T \\ \Delta\vec{u}_2 &= [\Delta\varepsilon]^T \end{aligned} \tag{9}$$

In this reduced-order model, the output vector is set up such that it contains only the states themselves or contains quantities which are a function of only the states. Therefore, the matrices D_1 and D_2 given in Equation 8 are eliminated from the model structure. In addition, note that while the controller uses a reduced-order linear model, its performance was ultimately tested with the full nonlinear model given by Equation 6.

Inner Loop CLAW

A diagram of the inner loop CLAW is shown in Figure 6. In the inner loop, the response type to pilot input is designed for Attitude Command Attitude Hold (ACAH) in the roll and pitch axis, where pilot input commands a change in roll and pitch attitudes ($\Delta\phi_{cmd}$ and $\Delta\theta_{cmd}$) and returns to the trim values when input is zero. The heave axis response type is designed for Rate Command Height Hold (RCHH), where pilot input commands a change in rate-of-climb and holds current height when the rate-of-climb is zero. The yaw axis response type is designed for Rate Command Direction Hold (RCDH), where pilot input commands a change in yaw rate and holds current heading when yaw rate is zero. These are based on ADS-33E specifications for hover and low-speed forward flight ($V \leq 45$ knots) (Ref. 16).

The commanded values (shown in Figure 6) are given by

$$\Delta\vec{y}_{inner,cmd} = \begin{bmatrix} \Delta\phi_{cmd} \\ \Delta\theta_{cmd} \\ \Delta V_{Z_{cmd}} \\ \Delta r_{cmd} \end{bmatrix} \tag{10}$$

They are subsequently passed through command filters, which generate the reference trajectories ($\Delta\vec{y}_{ref}$) and their derivatives ($\dot{\Delta\vec{y}}_{ref}$) (see Figure 6). The parameters of the command filter were selected to meet Level 1 handling qualities specifications (bandwidth and phase delay) given by ADS-33E for small amplitude response in hover and low-speed forward flight (Ref. 16). Table 1 shows the parameters used in the command filters in the inner loop CLAW, where the roll and pitch axes use second-order filters and the heave and yaw axes use first-order filters.

Table 1: Inner Loop Command Filter Parameters

Command Filter	ω_n (rad/sec)	ζ	τ (sec)
Roll	2.5	0.8	-
Pitch	2.5	0.8	-
Heave	-	-	2
Yaw	-	-	0.4

In dynamic inversion, the technique of input-output feedback linearization is used, where the output equation ($\Delta\vec{y}_{inner}$ in Equation 11) is differentiated until the input appears explicitly in the derivative (Refs. 14, 17). The inversion model implemented in the controller uses the 8-state vector given by Equation 9. Writing the reduced-order linear model in state space form, we have

$$\begin{aligned} \dot{\Delta\vec{x}}_r &= A_r\Delta\vec{x}_r + B_{1r}\Delta\vec{u}_{1r} + B_{2r}\Delta\vec{u}_2 \\ \Delta\vec{y}_{inner} &= C_r\Delta\vec{x}_r \end{aligned} \tag{11}$$

where the A_r matrix is 8x8, B_{1r} is 8x4, B_{2r} is 8x1, C_r matrix is 4x8, and the output vector $\Delta\vec{y}_{inner}$ is 4x1.

Applying dynamic inversion on Equation 11 results in the following control law

$$\begin{aligned} \Delta\vec{u}_{1r} = \left[C_rA_r^{k-1}B_{1r}\right]^{-1} \Bigg(\nu - \left[C_rA_r^k\right]\Delta\vec{x}_r \\ - \left[C_rA_r^{k-1}B_{2r}\right]\Delta\vec{u}_2 \Bigg) \end{aligned} \tag{12}$$

where k = 2 for the roll and pitch axes, and k = 1 for the heave and yaw axes. The term $\left[C_rA_r^{k-1}B_{2r}\right]\Delta\vec{u}_2$ is an additional feedforward component due to the morphing input. The process of feeding the morphing control into the inversion is similar to applications of DI for aircraft with redundant controls (Refs. 19, 20).

The term ν is known as the "pseudo-command" vector or an auxiliary input vector, shown in Figure 6. The psuedo-command vector is a sum of feedforward and feedback components. It is defined as

$$\nu = \begin{bmatrix} \nu_\phi \\ \nu_\theta \\ \nu_{V_Z} \\ \nu_r \end{bmatrix} = \dot{\Delta\vec{y}}_{ref} + [K_P\ K_D\ K_I] \begin{bmatrix} e \\ \dot{e} \\ \int e\, dt \end{bmatrix} \tag{13}$$

where the error vector, denoted as e (see Figure 6) is given by

$$e = \Delta\vec{y}_{ref} - \Delta\vec{y}_{inner} \tag{14}$$

The variables K_P,K_D, and K_I indicate the proportional, derivative, and integral gains in a PID compensator.

Note that the application of dynamic inversion in Equation 11 is carried out in the body reference frame. In Equation 13, the pseudo-commands ν_ϕ, ν_θ, and ν_r are prescribed in the body frame, while ν_{V_Z} is in the inertial frame. Therefore, a transformation was introduced to change the heave axis pseudo-command to the body frame (Ref. 18) prior to inversion, and is given by

$$\nu_w = \frac{\nu_{V_Z} + u\dot{\theta}\cos\theta}{\cos\theta\cos\phi} \tag{15}$$

If the reduced-order model given by Equation 11 were a perfect representation of the flight dynamics, the resulting system after inversion would behave like a set of integrators and the pseudo-command vector would not require any feedback compensation. In practice, however, errors between reference and measured values arise due to higher-order vehicle dynamics and/or external disturbances and therefore require feedback to ensure stability.

The PID compensator gains are selected to ensure that the tracking error dynamics due to disturbances or modeling error are well regulated. A typical choice for the gains is that the error dynamics be on the same order as that of the command filter (ideal) model for each axis. Table 2 shows the compensator gain values used in each axis.

Table 2: Inner Loop Error Compensator Gains

	K_P	K_D	K_I
Roll	10 (1/sec^2)	5.75 (1/sec)	4.6875 (1/sec^2)
Pitch	10 (1/sec^2)	5.75 (1/sec)	4.6875 (1/sec^2)
Heave	1 (1/sec)	0	0.25 (1/sec)
Yaw	1 (1/sec)	0	6.25 (1/sec)

Finally, the vector $\Delta\vec{u}_{1r}$ from Equation 12 is added to the trim values of $\vec{u}_{1r}$ before being passed into the control mixing unit of the aircraft.

Outer Loop CLAW

In order to maintain trimmed forward flight, an outer loop autopilot is designed to regulate lateral (V_Y) and longitudinal (V_X) ground speed while the aircraft is morphing. A schematic of the outer loop CLAW is shown in Figure 7. Note that the overall structure is similar to the inner loop. The response type for the outer loop is translational rate command, position hold (TRC/PH), where pilot inputs command a change in ground speed and hold current inertial position when inputs are zero. With the implementation of the outer loop, the pilot input does not directly command $\Delta\phi_{cmd}$ and $\Delta\theta_{cmd}$ as in the inner loop CLAW. Rather, they are indirectly commanded through the desired ground speeds (see Figure 5).

The commanded values in the outer loop (shown in Figure 7) are given by

$$\Delta\vec{y}_{outer,cmd} = \begin{bmatrix} \Delta V_{X_{cmd}} \\ \Delta V_{Y_{cmd}} \end{bmatrix} \tag{16}$$

and passed through first-order command filters. Similar to the inner loop, the parameters of the command filter are selected based on ADS-33E specifications in hover and low-speed forward flight (Ref. 16).

Table 3: Outer Loop Command Filter Parameters

Command Filter	τ (sec)
Longitudinal (V_X)	2.5
Lateral (V_Y)	2.5

In the outer loop, to achieve the desired ground speeds, the required pitch and roll attitude command input to the inner loop (Equation 10) is determined through model inversion (Ref. 19). A simplified linear model of the lateral and longitudinal dynamics is extracted from Equation 11 and is given by

$$\begin{aligned} \Delta\dot{\vec{x}}_{r,outer} &= A_{TRC}\Delta\vec{x}_{r,outer} + B_{TRC}\begin{bmatrix} \Delta\phi_{cmd} \\ \Delta\theta_{cmd} \end{bmatrix} \\ \Delta\vec{y}_{outer} &= \begin{bmatrix} \Delta V_X \\ \Delta V_Y \end{bmatrix} = C_{TRC}\Delta\vec{x}_{r,outer} \end{aligned} \tag{17}$$

with A_{TRC}, B_{TRC}, and $\Delta\vec{x}_{r,outer}$ defined as

$$\begin{aligned} A_{TRC} &= \begin{bmatrix} X_u & X_v \\ Y_u & Y_v \end{bmatrix} \\ B_{TRC} &= \begin{bmatrix} 0 & -g \\ g & 0 \end{bmatrix} \\ \Delta\vec{x}_{r,outer} &= \begin{bmatrix} \Delta u \\ \Delta v \end{bmatrix} \end{aligned} \tag{18}$$

where u and v are body-axis velocities, X_u, X_v, Y_u, and Y_v are stability derivatives and g is the gravitational acceleration. Applying dynamic inversion on this model results in the following control law

$$\begin{bmatrix} \Delta\phi_{cmd} \\ \Delta\theta_{cmd} \end{bmatrix} = (C_{TRC}B_{TRC})^{-1}\left(\nu - C_{TRC}A_{TRC}\Delta\vec{x}_{r,outer}\right) \tag{19}$$

The pseudo-command vector, $\nu = \begin{bmatrix} \nu_{V_X} \\ \nu_{V_Y} \end{bmatrix}$, is defined similarly to Equation 13, with the error dynamics also defined in a manner similar to that of the inner loop. The PID compensator gains for the outer loop are given in Table 4.

Table 4: Outer Loop Error Compensator Gains

	K_P (1/sec)	K_D	K_I (1/sec)
Lateral (V_Y)	0.8	0	0.16
Longitudinal (V_X)	0.8	0	0.16

RPM Governor

Rotor morphing is certainly expected to impact the rotational degree of freedom (Ω). On the UH-60A and in the GenHel model, the rotor RPM is regulated by a complex, nonlinear engine Electrical Control Unit (ECU) (Ref. 7). Since a simplified modeling of the propulsion dynamics is used in this study, a simple PI controller, with collective input feed-forward from the inner loop CLAW, is implemented to regulate the rotor RPM via the throttle input, which is mapped to the fuel flow state (χ_f). The controller is similar in structure to the one given by Kim (Ref. 21). A schematic of the RPM Governor is shown in Figure 8. In Figure 8, the gains K_P and K_I were empirically selected. The collective feed-forward gain, K_C, was approximated using a mapping between throttle and collective input, based on trim sweep results of the baseline model. Table 5 shows the gains used in the governor.

Table 5: RPM Governor Gains

	K_P (%/(rad/sec))	K_I (%/(rad/sec))	K_C (nd)
Ω	6	1.5	1.2

RESULTS

Sea Level - 40 and 120 knots

The aircraft was trimmed at speeds of 40 and 120 knots with a gross weight of 20,000 lbs at sea-level. The chord between 63% and 83% of the blade span was increased by 20% at a deployment angle of $\eta = 2$ degrees over 60 seconds. Figures 9 to 12 show simulation results at 40 knots. The aircraft steady thrust and main rotor torque (Figure 9(c)) associated with the chord extension. The thrust (Figure 9(b)) is observed to be regulated well and main rotor torque (Figure 9(c)) increases slightly over the duration of morphing, primarily due to higher profile drag on the blade sections with the extended TEP. Figure 10 shows the variation in primary controls and aircraft roll and pitch attitude and Figure 11 shows the variation in rotor flapping, over the duration of the morphing. A decrease of 0.4 degrees in rotor collective pitch (Figure 10(c)) is observed because of the chord extension. The tail rotor pitch (Figure10(d)) increases slightly because of the higher rotor torque. The larger lateral force due to increase in tail rotor thrust and increased roll moment it generates due to its location above the CG affect the lateral force and roll moment equilibrium. Consequently, there is a slight increase in lateral flapping (Figure 11(b)) and lateral cyclic pitch (Figure 10(a)), while the roll attitude remains relatively unchanged (Figure 10(e)). Due to the tail rotor cant angle on the UH-60A (Ref. 7), the increase in tail rotor thrust also increases the nose-down pitching moment on the aircraft. Consequently, the forward tilt of the tip path plane (Figure 11(c)) reduces slightly to compensate, with the pitch attitude remaining relatively unchanged (Figure 10(f)). Figure 12 shows time histories of the aircraft velocities, which are well regulated by the controller. Recall that the ground speeds V_X and V_Y are regulated by the outer loop and vertical speed V_Z by the inner loop.

Figures 13-14 show simulation results at a high speed of 120 knots, with chord extension over 60 seconds (Figure 13(a)). Figures 13(b) and 13(c) show variation in aircraft steady thrust and torque. Again, thrust is regulated well and torque increases over the duration of morphing due to higher profile drag with extended chord. Figure 14 shows the variation in primary controls and attitudes. The rotor collective pitch (Figure 14(c)) decreases again by about 0.4 degrees and trends in the remaining controls are dictated by the change in required tail rotor pitch, as they were at 40 knots. It was verified that the flapping response followed similar trends and inertial velocities were regulated well (results not shown in paper).

6K, 95 °F - 40 knots

The aircraft was trimmed at a speed of 40 knots with a gross weight of 20,000 lbs at an altitude of 6000 ft and a temperature of 95 °F (hot and high condition). The chord was again increased by 20% over 60 seconds (Figure 15(a)). Figures 15(b) and 15(c) show the variation in aircraft steady thrust and main rotor torque associated with the chord extension. Thrust is regulated well and the main rotor torque decreases slightly because of reductions in profile drag associated with the aircraft getting further away from stall. Figure 16 shows the variation in controls and attitudes of the aircraft. The rotor collective pitch decreases about 0.6 degrees (Figure 16(c)) due to the chord extension. There is a slight reduction in the tail rotor pitch because of the torque decrease, which again affects lateral force and roll moment equilibrium. The lower tail rotor pitch reduces the right lateral force and right roll moment, which is counteracted by the slightly reduced roll left attitude (Figure 16(e)), while the lateral flap remains relatively unchanged (Figure 17(b)). Similarly, a lower tail rotor thrust reduces the nose-down pitching moment, which is counteracted by the slight increase in longitudinal tilt of the tip path plane (Figure 17(c)), while the pitch attitude remains relatively unchanged (Figure 16(f)). The inertial velocities were verified to be regulated well over the duration of morphing (results not shown).

Rate of Morphing and Asynchronous Deployment

The previous sections considered chord extension at different flight conditions. In this section, questions addressed are: (1) the impact of reducing the morphing duration across all four blades and (2) the effect of asynchronous morphing across the blades.

Figures 18(b)-18(d) show plots of main rotor torque and cyclic controls for morphing durations of 60, 30, and 15 seconds (Figure 18(a)) at 40 knots, sea-level conditions. While the transients are slightly sharper for lower morphing durations, the controller is robust to morphing rates and does not require changes to gains or model updates.

In Figure 18 (and all preceding simulations) the morphing input was applied identically over all four blades. Due to actuator or control system problems, three specific cases of interest are identified where this may not be so: (1) the chord extension on one of the blades may deploy to a different magnitude from the others, (2) the chord extension on one of the blades may deploy to the correct magnitude but over a longer duration of time, and (3) the chord extension on one of the blades deploys to the correct magnitude and over the correct duration of time but is temporally offset (for example, delayed relative to the other blades). While case 1 is expected to result in persistent 1/rev vibratory loads associated with an unbalanced rotor, cases 2 and 3 would be expected to result in some transient loads and due to unbalance during the morphing process, which eventually die out when all the blades have eventually reached the commanded steady state chord extension amplitudes.

Case 3 is examined here and Figure 19(a) shows the deployment of the TEP delayed by 15 seconds for one of the blades and Figures 19(b)-19(d) show the aircraft thrust and cyclic swashplate controls. The controller commands a small 1/rev input in addition to the steady component to the swashplate. In the simulation model, the outputs from the control mixing block go through actuator servos (shown in Figure 5). These are second-order low-pass filters, based on the GenHel model (Ref. 11), with a bandwidth of approximately 11.3 Hz. While this high bandwidth allows the 1/rev inputs in the fixed-frame to pass through without much attenuation, such inputs may not be desirable due to prohibitive power requirements to actuate the swashplate.

CONCLUSIONS

The present study focused on the flight simulation and control of a helicopter undergoing rotor chord morphing. A model-following dynamic inversion controller is implemented with inner and outer loop control laws (CLAWS) and chord morphing is introduced as an additional feed-forward input to the inner loop CLAW. Simulation results are presented for a chord-morphing variant of a UH-60A Black Hawk helicopter at a gross weight of 20,000 lbs. Starting with the baseline rotor blade, the chord is increased from 63% to 83% by means of a trailing-edge plate (TEP) extension at a deployment angle of $\eta = 2$ degrees. From the results presented, the following conclusions can be drawn:

1. The dynamic inversion (DI) controller regulates the operating state of the aircraft well over the nominal 60 second duration of chord morphing and maintains its effectiveness even when the duration is reduced to 15 seconds.

2. Chord morphing at sea-level conditions resulted in slightly increased torque requirements due to additional profile drag on the blade sections with the extended chord. In the hot-and-high condition, chord morphing slightly reduces torque due to lower profile drag as the rotor's operating state moves further away from stall.

3. The required rotor collective pitch reduces by about 0.4 degrees in sea-level conditions and by about 0.6 degrees at hot-and-high conditions. The trends in the cyclic pitch controls and flapping response are governed by changes in the tail rotor thrust, which affects the lateral and longitudinal equilibrium of the aircraft.

4. Asynchronous morphing on the blades resulted in small 1/rev inputs to the swashplate from the controller. Despite the small amplitude, such inputs may not be desirable due to power limitations.

Author contact:
Jayanth Krishnamurthi, krishj@rpi.edu
Farhan Gandhi, gandhf@rpi.edu

REFERENCES

[1]Leon, O., Hayden, E., and Gandhi, F., "Rotorcraft Operating Envelope Expansion Using Extendable Chord Sections," , Proceedings of the 65^{th} AHS International Forum and Technology Display, Grapevine, TX, May 27-29, 2009.

[2]Khoshlahjeh, M., and Gandhi, F., "Extendable Chord Rotors for Helicopter Envelope Expansion and Performance Improvement," *Journal of the American Helicopter Society*, Vol. 59, (1), January 2014.
doi: 10.4050/JAHS.59.012007

[3]Barbarino, S., Gandhi, F., and Webster, S., "Design of Extendable Chord Sections for Morphing Helicopter Rotor Blades," *Journal of Intelligent Material Systems and Structures*, Vol. 22, (9), June 2011, pp. 891–905.
doi: 10.1177/1045389X11414077

[4]Gandhi, F., and Hayden, E., "Design, Development, and Hover Testing of a Helicopter Rotor Blade Chord Extension Morphing System," *Smart Materials and Structures*, Vol. 24, (3), 2015.
doi: 10.1088/09645-1726/24/3/035024

[5]Moser, P., Barbarino, S., and Gandhi, F., "Helicopter Rotor-Blade Chord Extension Morphing Using a Centrifugally Actuated Von Mises Truss," *Journal of Aircraft*, Vol. 5, (5), 51, pp. 1422–1431.
doi: 10.2514/1.C032299

[6]Krishnamurthi, J., and Gandhi, F., "Flight Simulation and Control of a Helicopter Undergoing Rotor Span Morphing," , Proceedings of the 41^{st} European Rotorcraft Forum, Munich, Germany, Sept. 1-4, 2015.

[7]Howlett, J.J., "UH-60A Black Hawk Engineering Simulation Program: Volume I - Mathematical Model," NASA CR-166309, 1981.

[8]Peters, D.A., and HaQuang, N., "Dynamic Inflow for Practical Applications," *Journal of the American Helicopter Society*, Vol. 33, (4), October 1988, pp. 64–66.

[9]Bailey, F.J., "A Simplified Theoretical Method of Determining the Characteristics of a Lifting Rotor in Forward Flight," NACA Report 716, 1941.

[10]Padfield, G.D., *Helicopter Flight Dynamics: The Theory and Application of Flying Qualities and Simulation Modeling*, Blackwell Publishing, second edition, 2007.

[11]Ballin, M.G., "Validation of a Real-Time Engineering Simulation of the UH-60A Helicopter," NASA TM-88360, 1987.

[12]Fletcher J.W., "A Model Structure for Identification of Linear Models of the UH-60 Helicopter in Hover and Forward Flight," NASA TM-110362, NASA, 1995.

[13]Bae, E.-S., and Gandhi, F., "CFD Analysis of High-Lift Devices on the SC-1094R8 Airfoil," , American Helicopter Society 67^{th} Annual Forum Proceedings, Virginia Beach, VA, May 3-5, 2011.

[14]Stevens, B.L. and Lewis, F.L., *Aircraft Control and Simulation*, John Wiley & Sons, second edition, 2003.

[15]Tischler, M.B. and Remple, R.K., *Aircraft and Rotorcraft System Identification: Engineering Methods with Flight Test Examples*, AIAA, second edition, 2012.

[16]Anonymous, "Aeronautical Design Standard Performance Specification, Handling Qualities Requirements for Military Rotorcraft," , ADS-33E-PRF, USAAMCOM, 2000.

[17]Slotine, J.E. and Li, W., *Applied Nonlinear Control*, Prentice-Hall Inc., 1991.

[18]Horn, J.F., and Guo, W., "Flight Control Design for Rotorcraft with Variable Rotor Speed," , Proceedings of the American Helicopter Society, 64^{th} Annual Forum, Montreal, Canada, April 29-May 1, 2008.

[19]Ozdemir, G.T., and Horn, J.F., "Simulation Analysis of a Flight Control Law with In-Flight Performance Optimization," Proceedings of the American Helicopter Society 68^{th} Annual Forum, Fort Worth, TX, May 1-3, 2012.

[20]Thorsen, A.T., Horn, J.F., and Ozdemir, G.T., "Use of Redundant Controls to Enhance Transient Response and Handling Qualities of a Compound Rotorcraft," Proceedings of American Helicopter Society 70^{th} Annual Forum, Montreal, Quebec, May 20-22, 2014.

[21]Kim, F.D., "Analysis of Propulsion System Dynamics in the Validation of a High-Order State Space Model of the UH-60," , AIAA/AHS Flight Simulation Technologies Conference, Hilton Head, S.C., August 24-26, 1992.

FIGURES

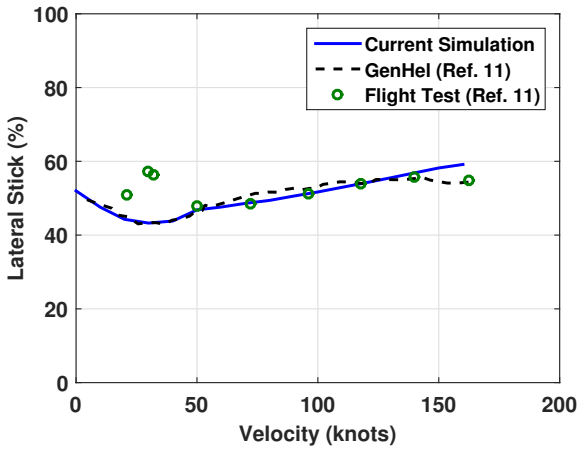

(a) Lateral Stick

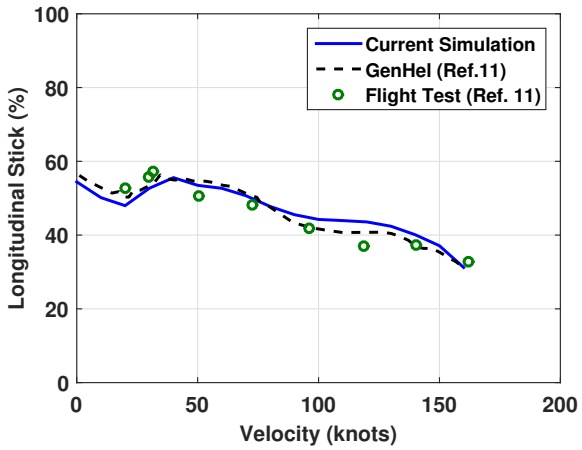

(b) Longitudinal Stick

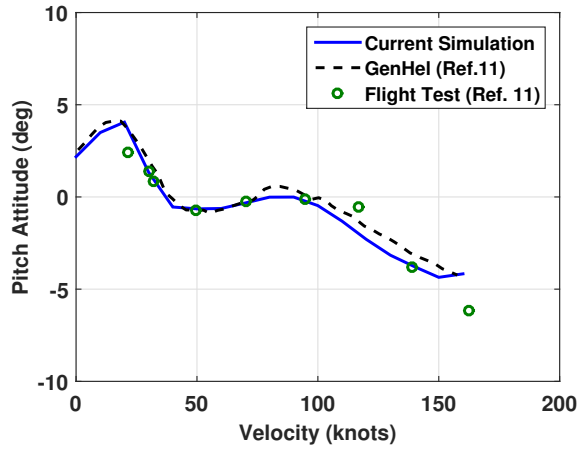

(c) Pitch Attitude

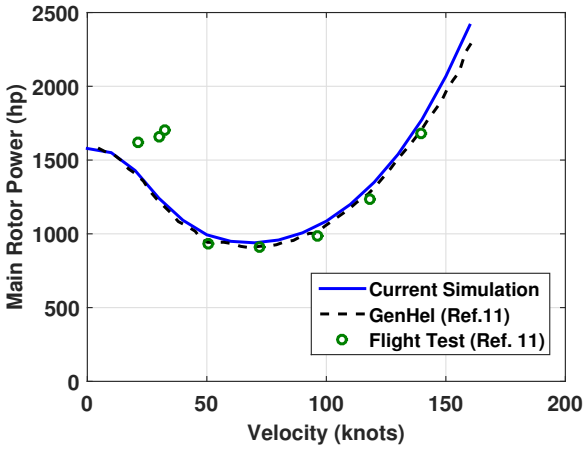

(d) Main Rotor Power

Fig. 1: Baseline UH-60A Trim Sweep Validation

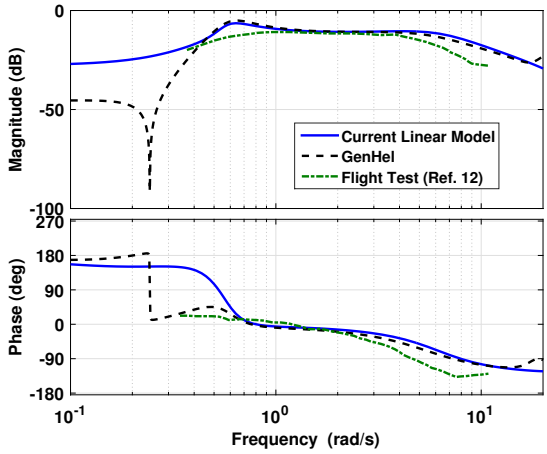

(a) Hover - $\Delta p/\Delta\delta_{lat}$

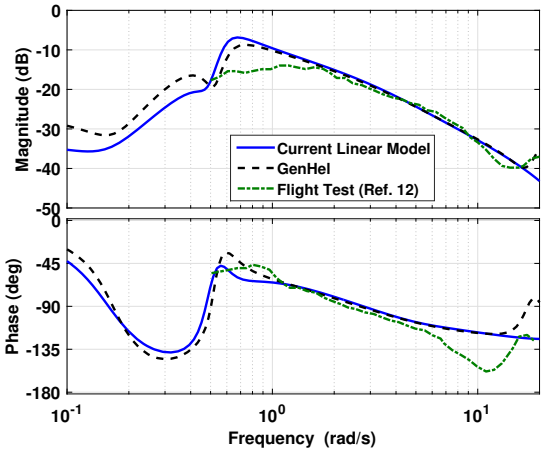

(b) Hover - $\Delta q/\Delta\delta_{long}$

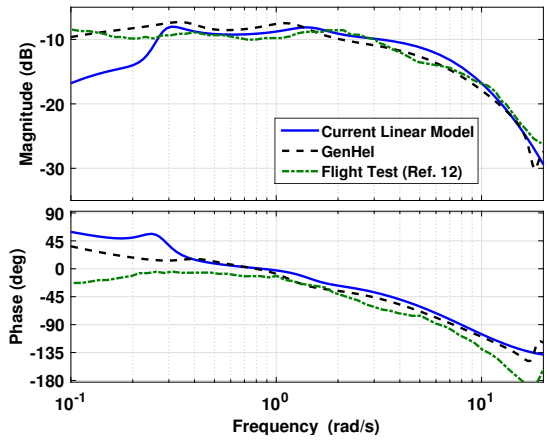

(c) 80 knots - $\Delta p/\Delta\delta_{lat}$

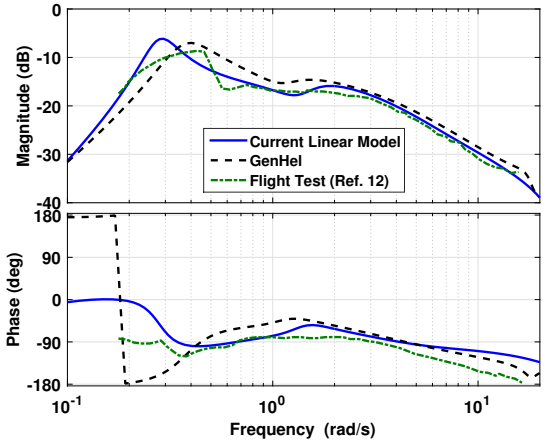

(d) 80 knots - $\Delta q/\Delta\delta_{long}$

Fig. 2: Baseline UH-60A Frequency Response Validation

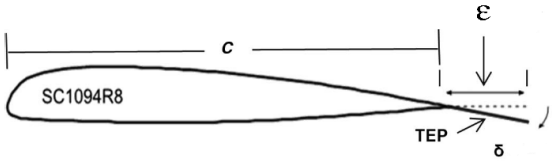

(a) TEP Extension - Airfoil

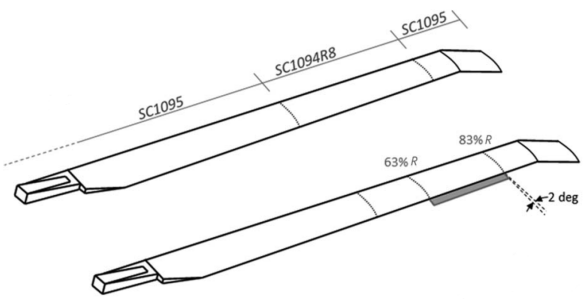

(b) TEP Extension - Blade

Fig. 3: Chord Extension Mechanism, Ref. 2

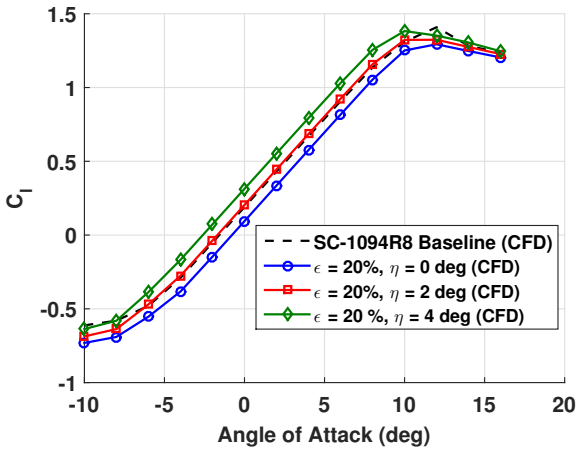

(a) Lift Coefficient

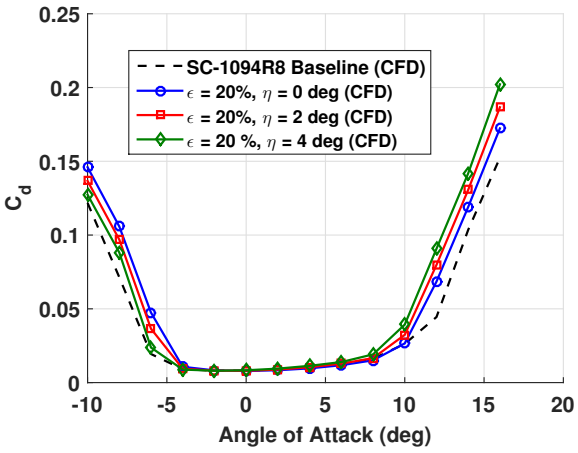

(b) Drag Coefficient

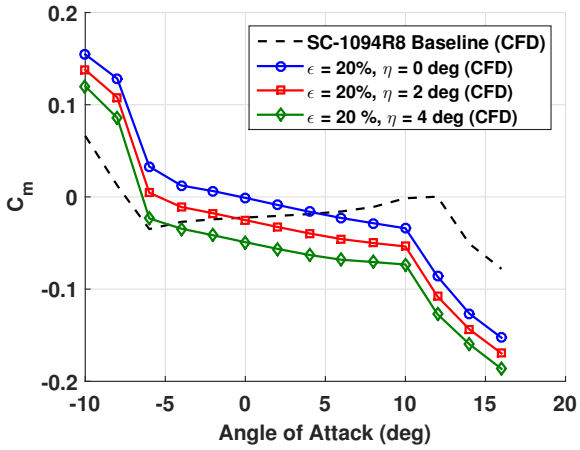

(c) Moment Coefficient

Fig. 4: SC-1094R8 - Aerodynamic coefficients for baseline and extendable TEP for Mach 0.4, Ref. 13

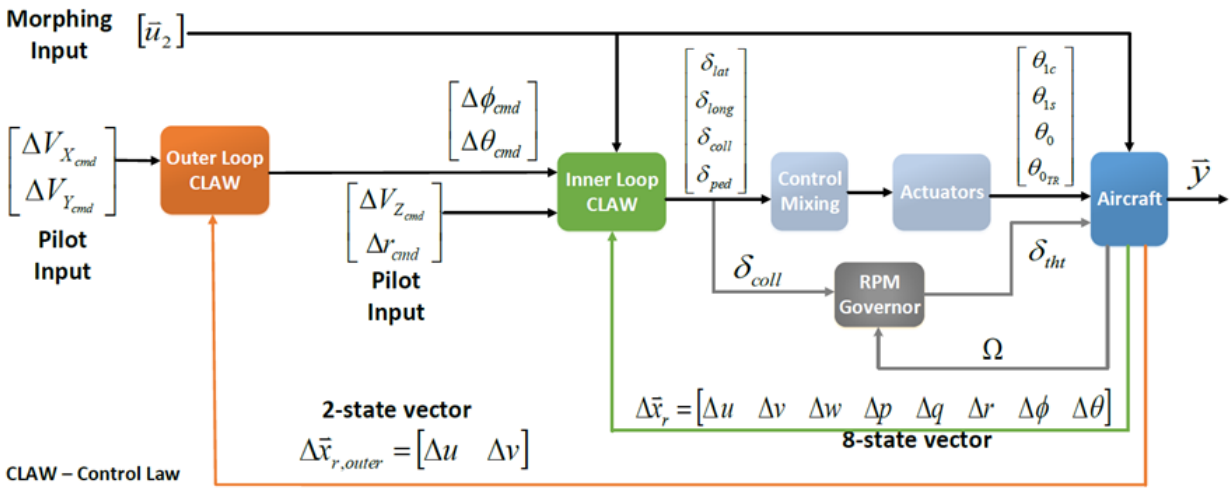

Fig. 5: Overview of the Control System

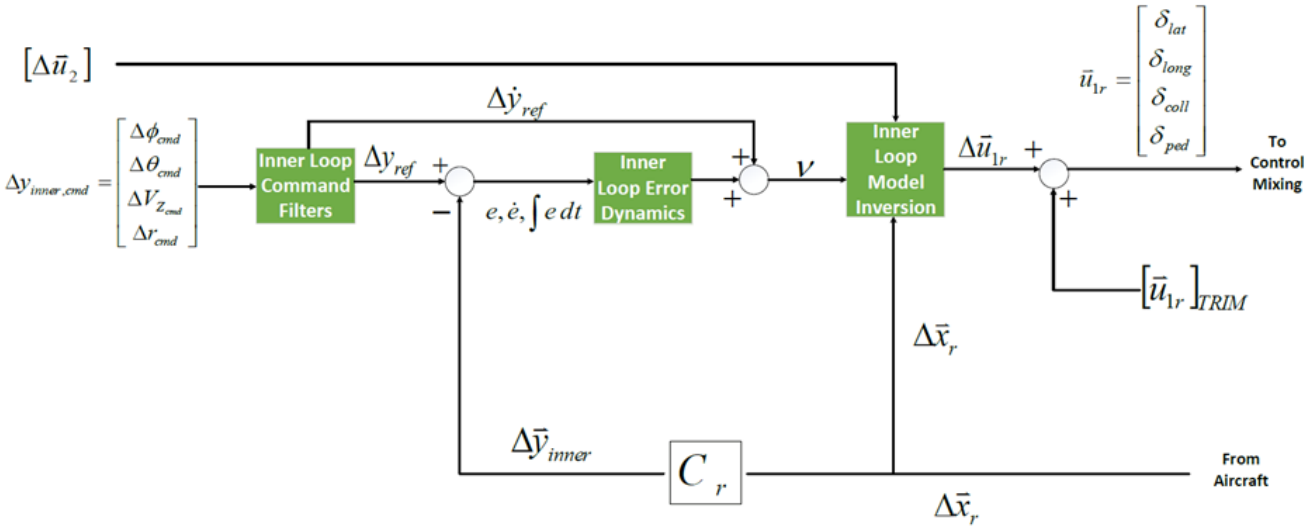

Fig. 6: Inner Loop CLAW

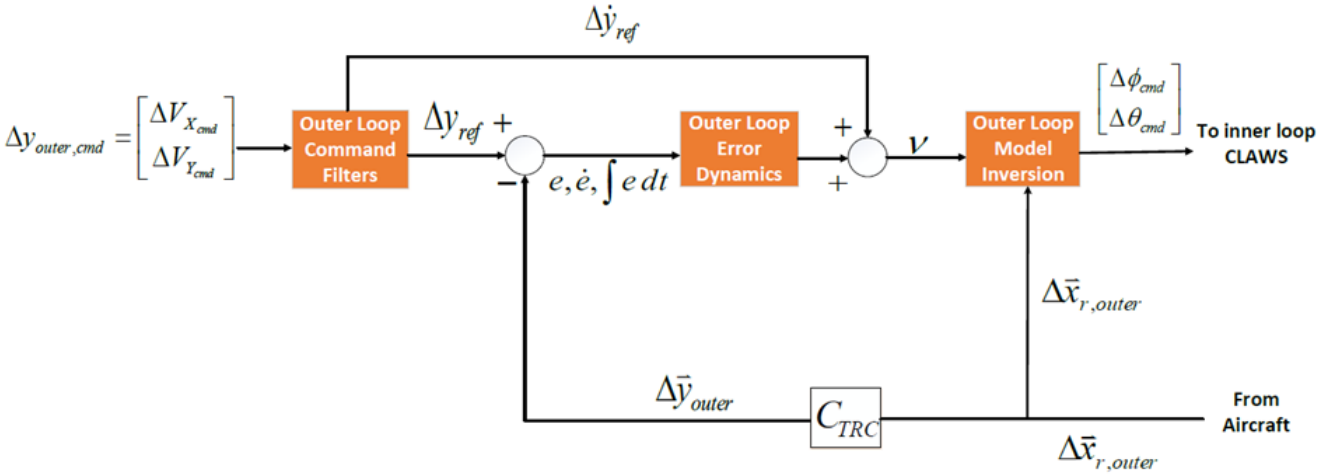

Fig. 7: Outer Loop CLAW

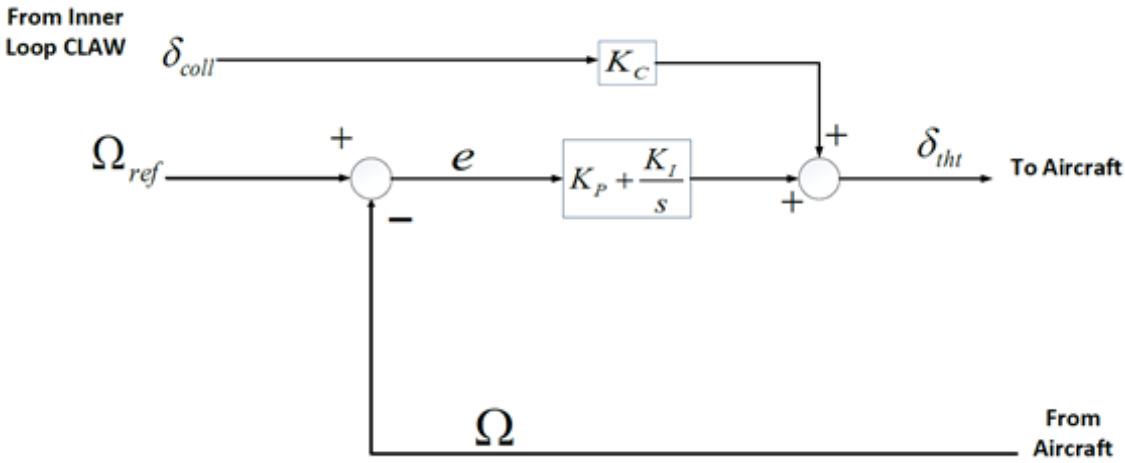

Fig. 8: RPM Governor

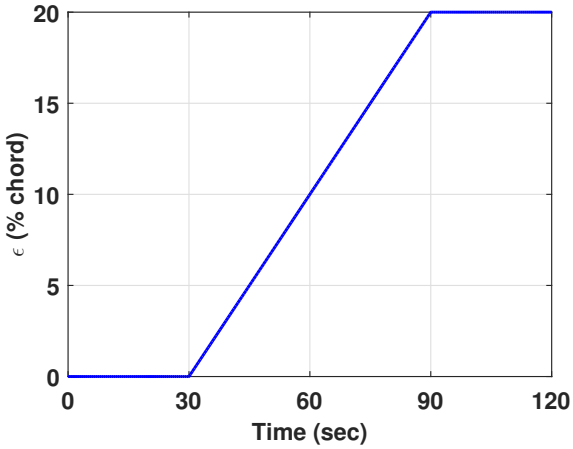

(a) TEP Extension

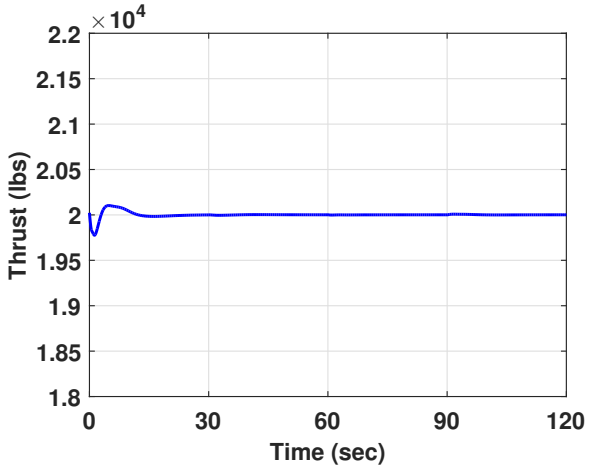

(b) Aircraft Thrust

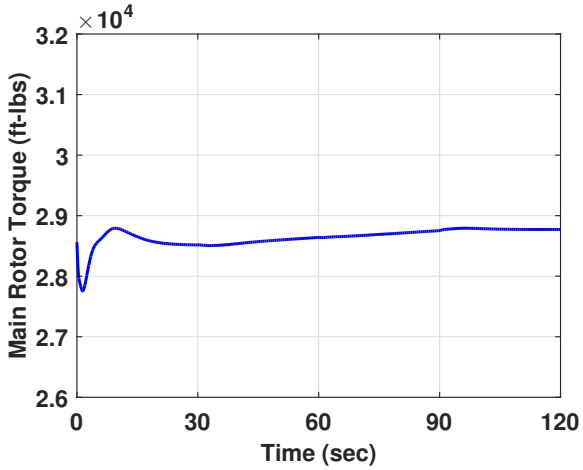

(c) Main Rotor Torque

Fig. 9: Chord Extension at 40 knots, Sea-level - TEP Extension, Thrust, and Torque

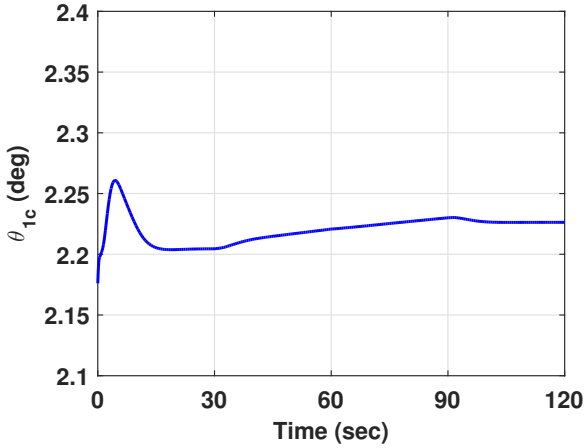

(a) Lateral Cyclic Pitch

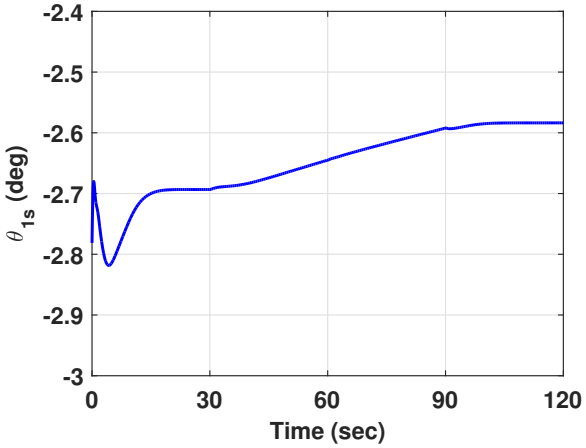

(b) Longitudinal Cyclic Pitch

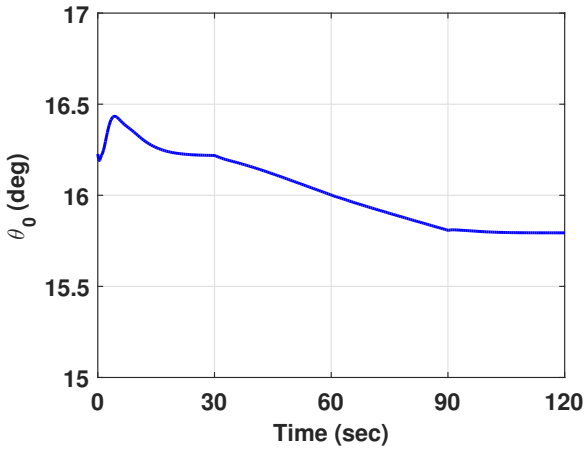

(c) Collective Pitch

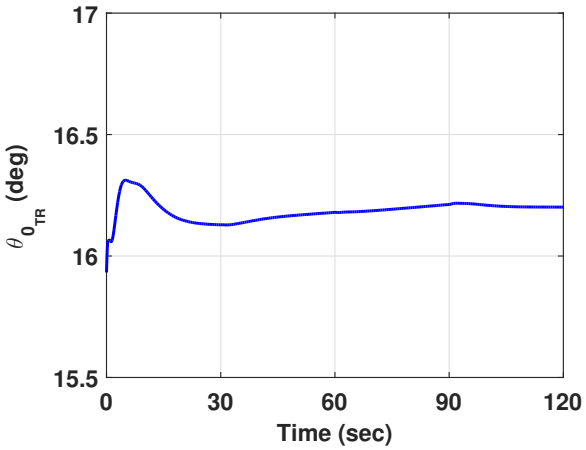

(d) Tail Rotor Pitch

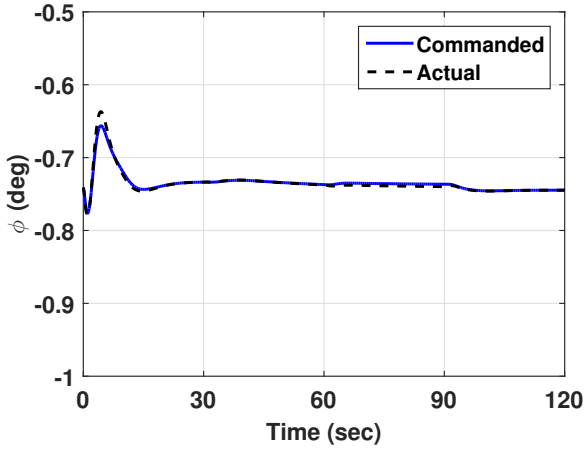

(e) Roll Attitude

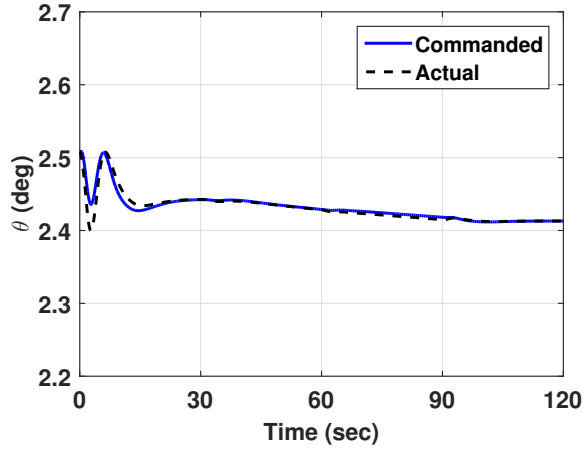

(f) Pitch Attitude

Fig. 10: Chord Extension at 40 knots, Sea-level - Controls and Attitudes (ϕ is positive roll right, θ is positive nose up)

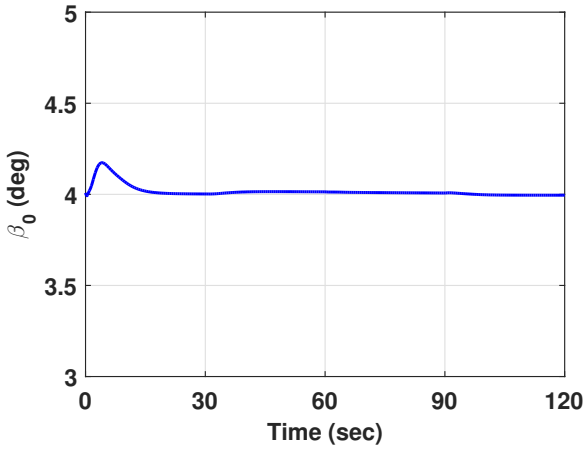

(a) Coning

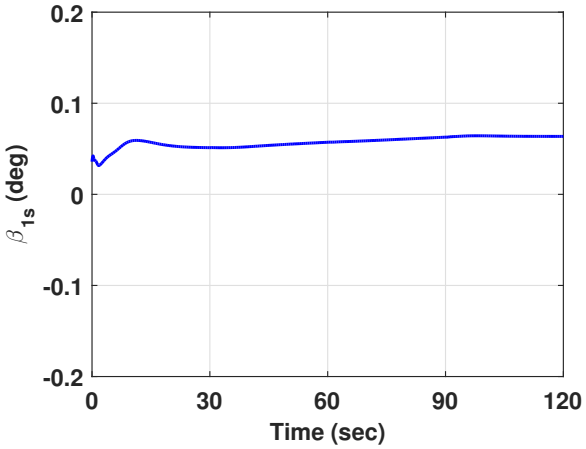

(b) Lateral Flapping

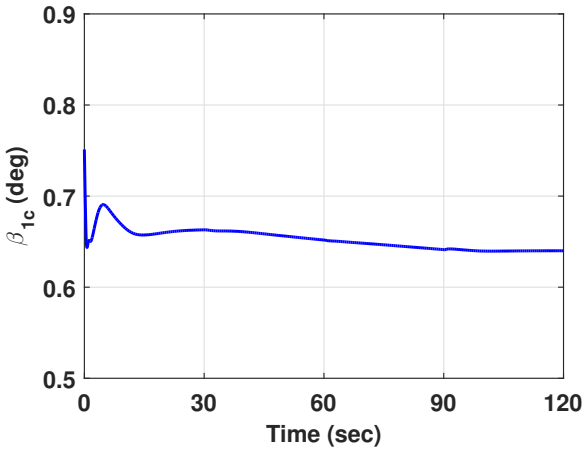

(c) Longitudinal Flapping

Fig. 11: Chord Extension at 40 knots, Sea-level - Flapping

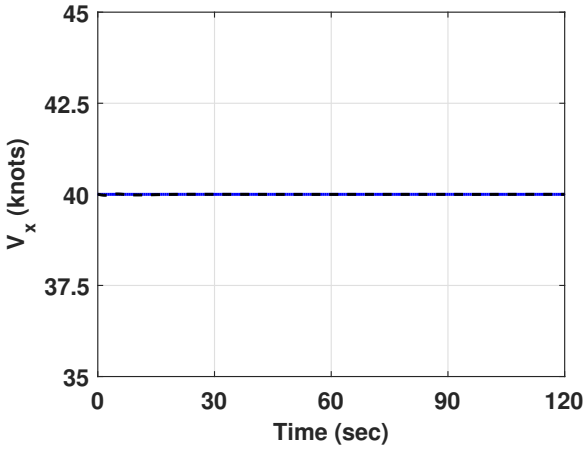

(a) Longitudinal Ground Speed

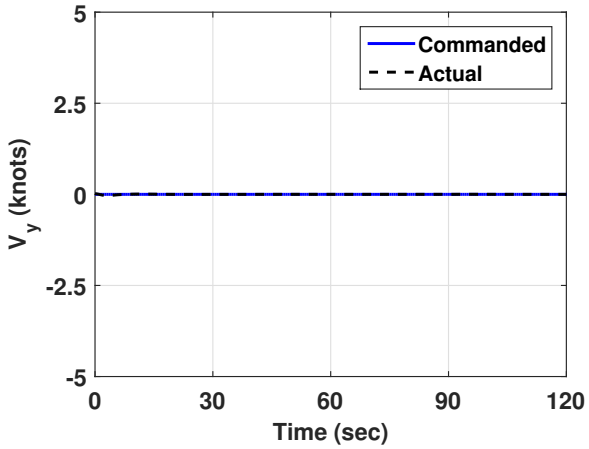

(b) Lateral Ground Speed

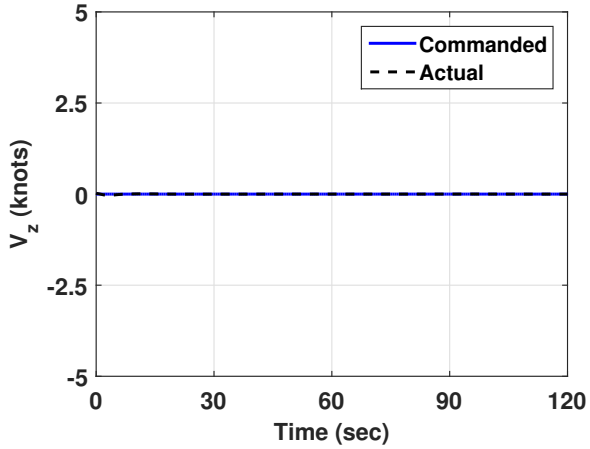

(c) Vertical Speed

Fig. 12: Chord Extension at 40 knots, Sea-level - Inertial Velocities

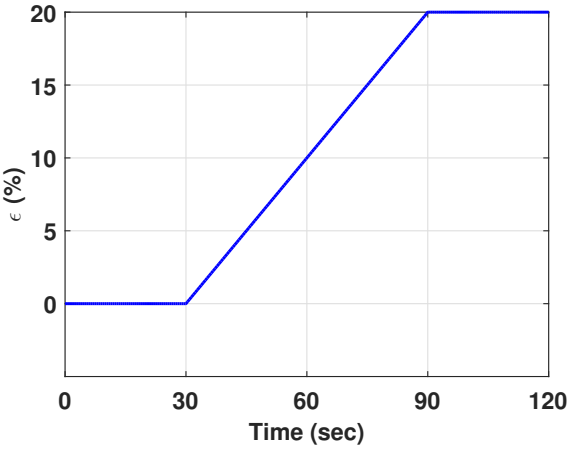

(a) TEP Extension

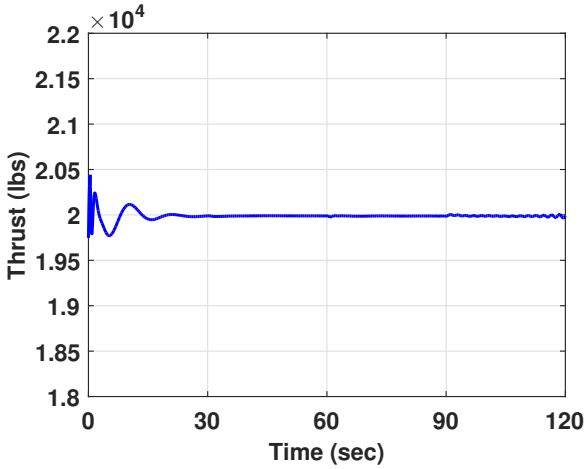

(b) Aircraft Thrust

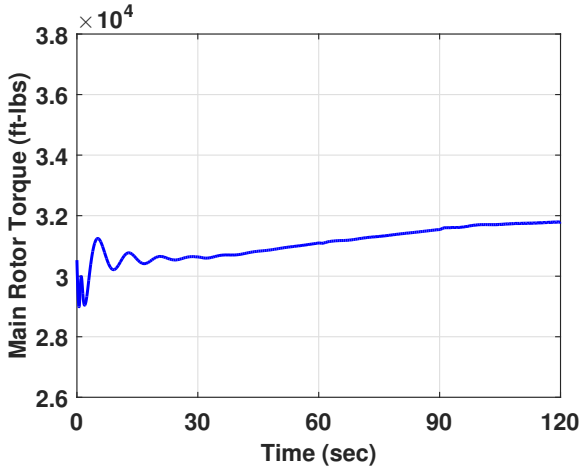

(c) Main Rotor Torque

Fig. 13: Chord Extension at 120 knots, Sea-level - TEP Extension, Thrust, and Torque

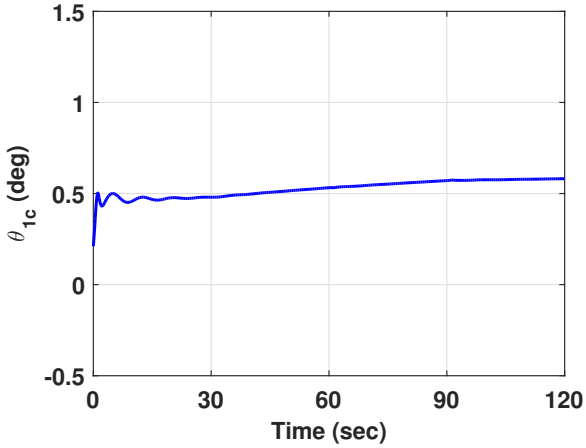

(a) Lateral Cyclic Pitch

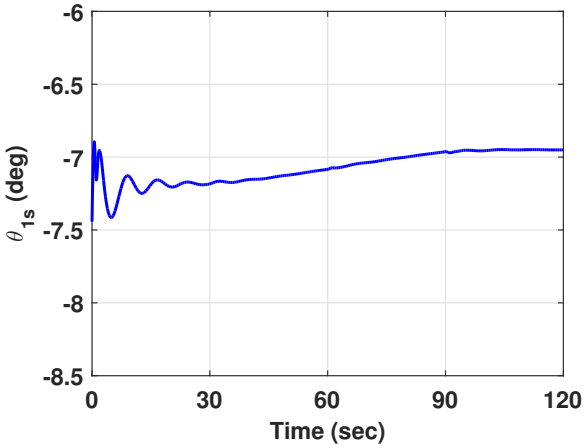

(b) Longitudinal Cyclic Pitch

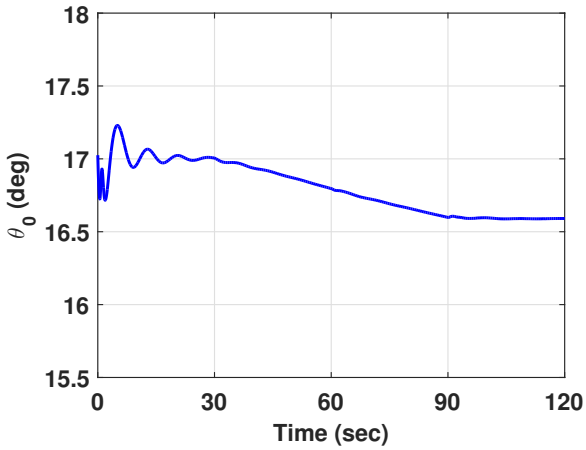

(c) Collective Pitch

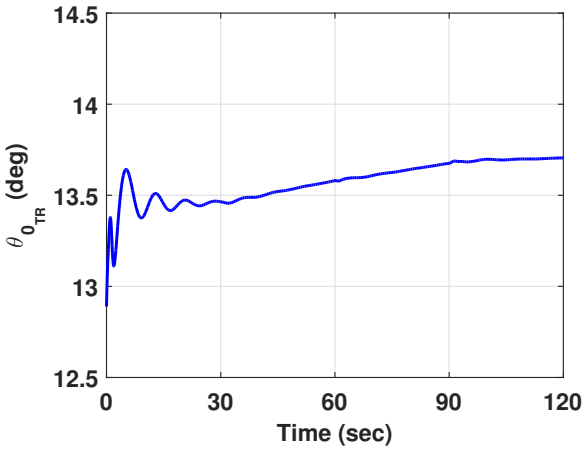

(d) Tail Rotor Pitch

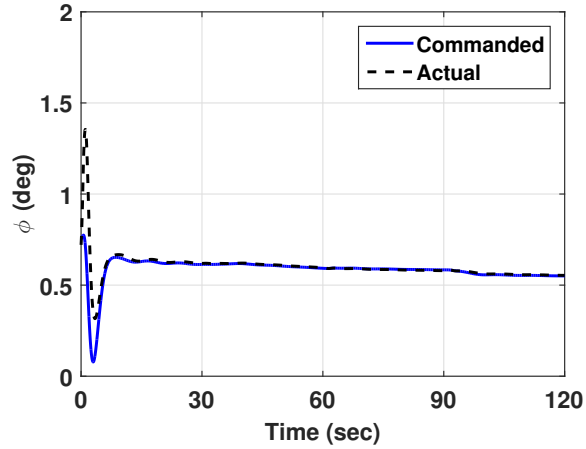

(e) Roll Attitude

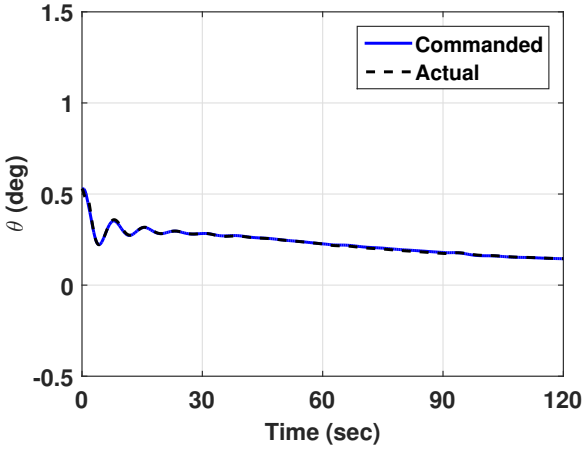

(f) Pitch Attitude

Fig. 14: Chord Extension at 120 knots, Sea-level - Controls and Attitudes (ϕ is positive roll right, θ is positive nose up)

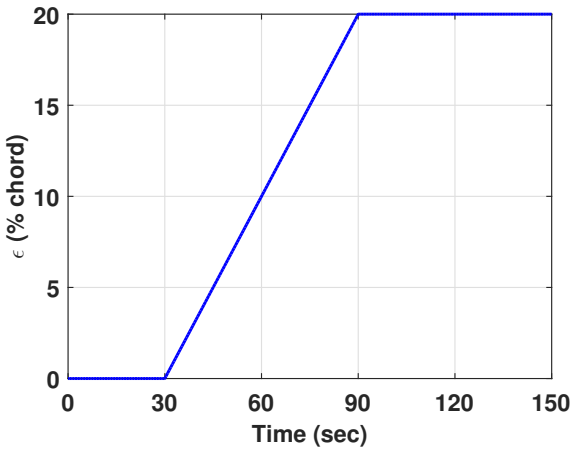

(a) TEP Extension

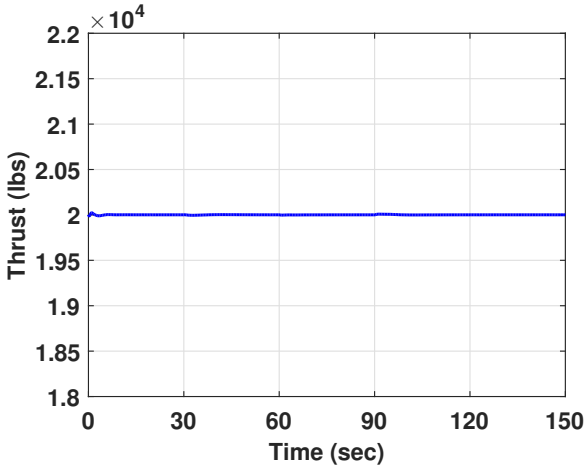

(b) Aircraft Thrust

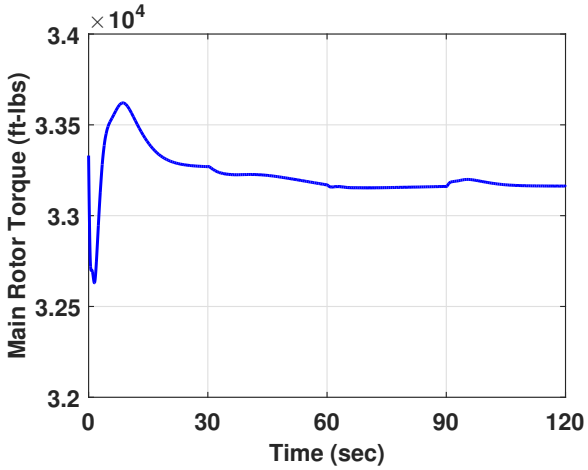

(c) Main Rotor Torque

Fig. 15: Chord Extension at 40 knots, 6000 ft, 95 °F. - TEP Extension, Thrust, and Torque

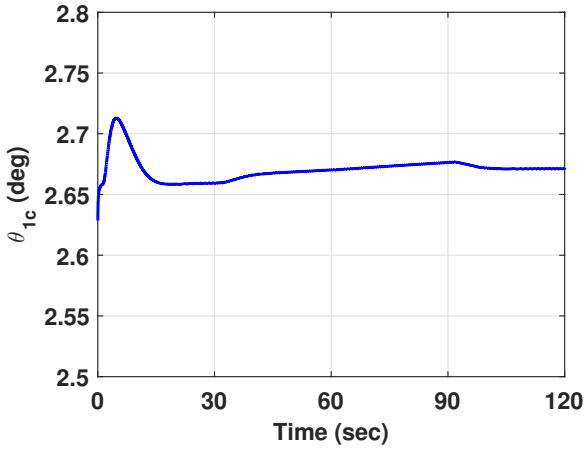

(a) Lateral Cyclic Pitch

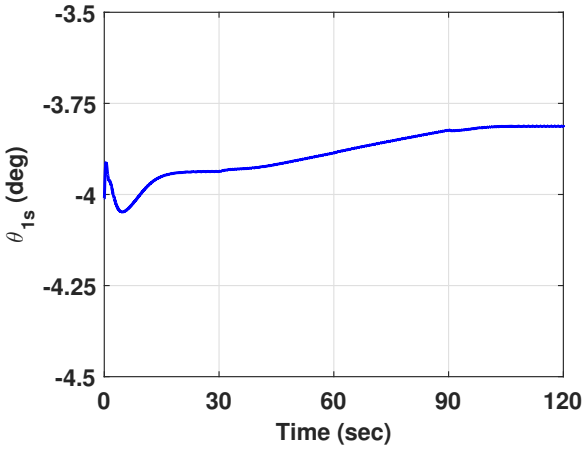

(b) Longitudinal Cyclic Pitch

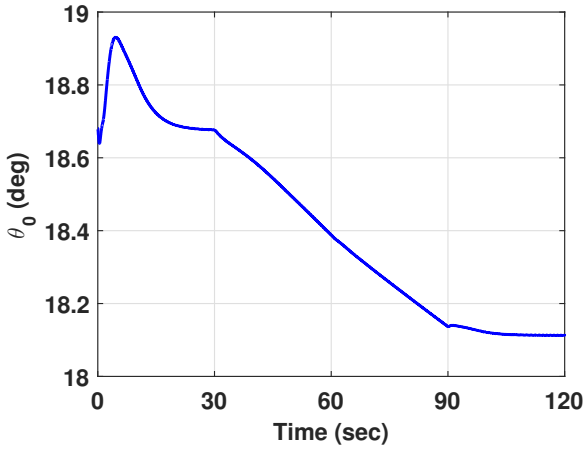

(c) Collective Pitch

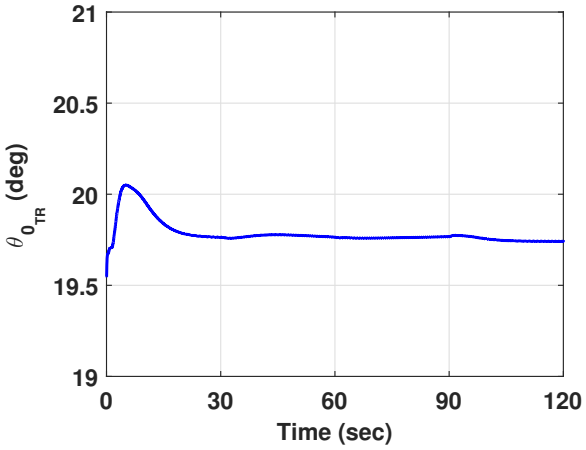

(d) Tail Rotor Pitch

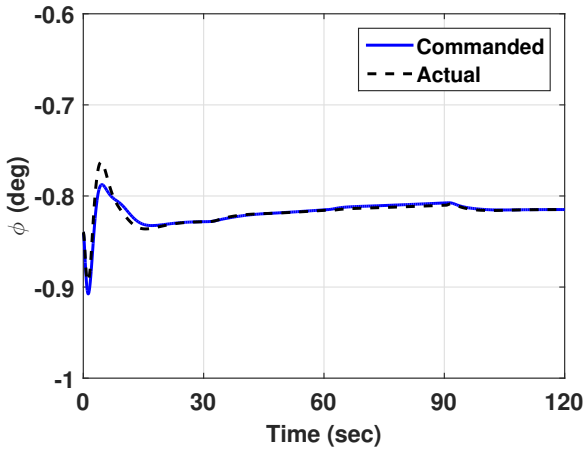

(e) Roll Attitude

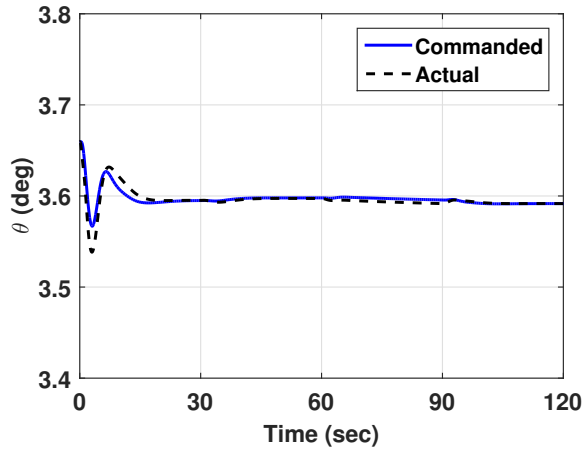

(f) Pitch Attitude

Fig. 16: Chord Extension at 40 knots, 6000 ft, 95 °F. - Controls and Attitudes

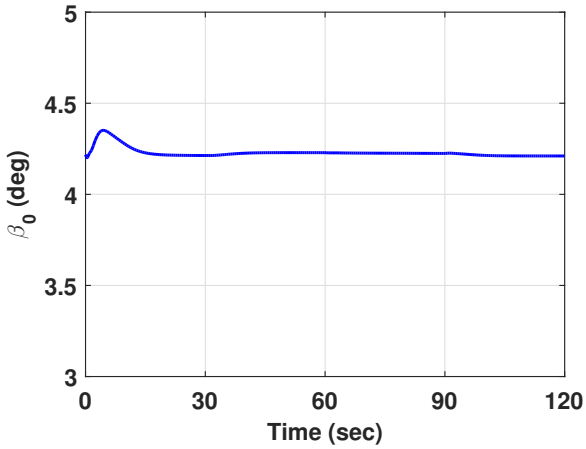

(a) Coning

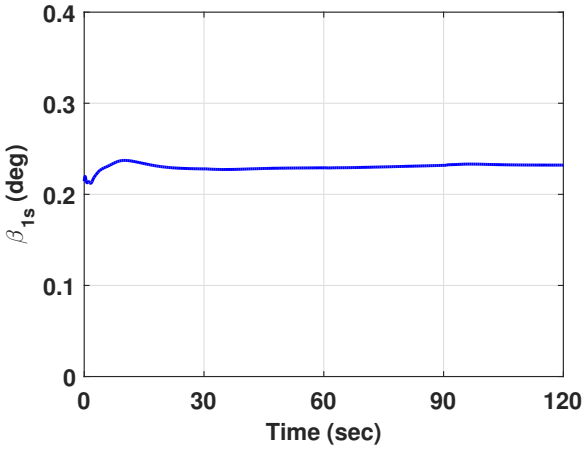

(b) Lateral Flapping

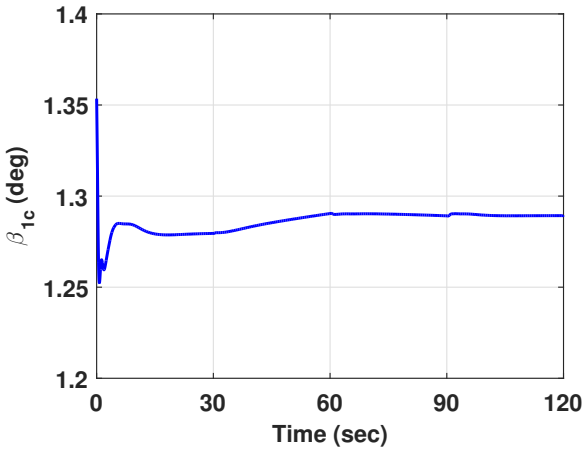

(c) Longitudinal Flapping

Fig. 17: Chord Extension at 40 knots, 6000 ft, 95 °F. - Flapping

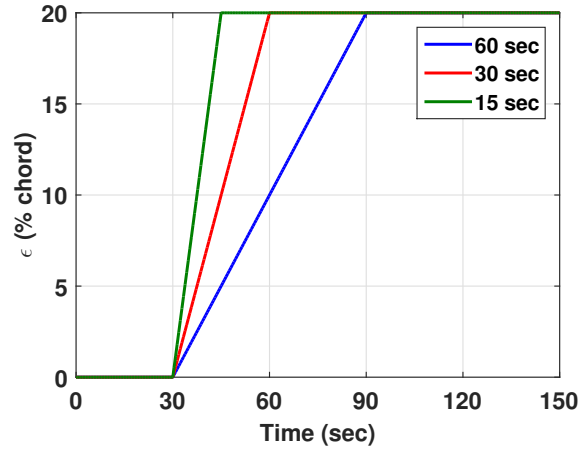

(a) TEP Extension

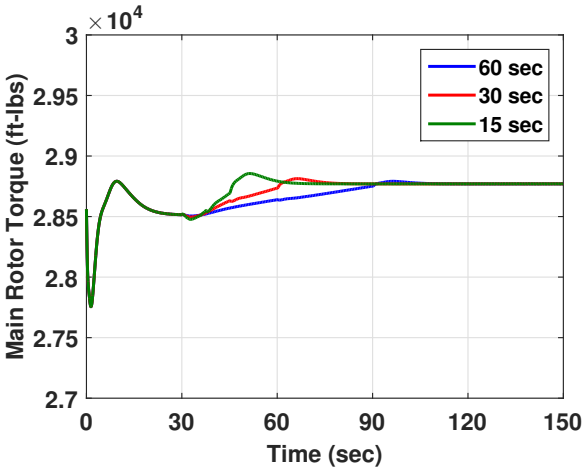

(b) Main Rotor Torque

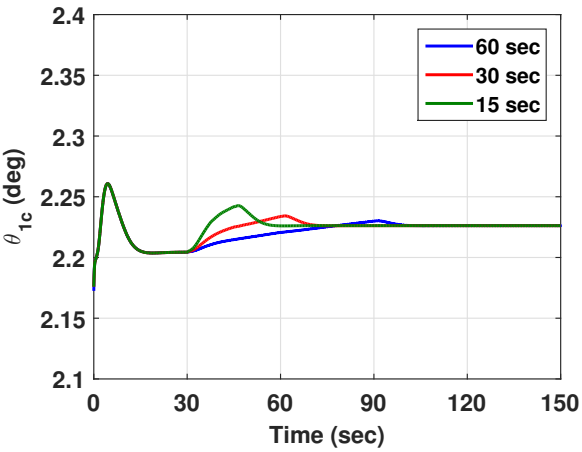

(c) Lateral Cyclic Pitch

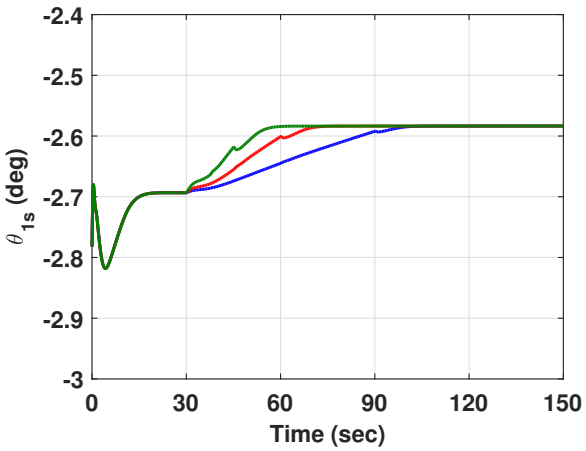

(d) Longitudinal Cyclic Pitch

Fig. 18: Variation in rate of chord morphing - 40 knots, sea-level

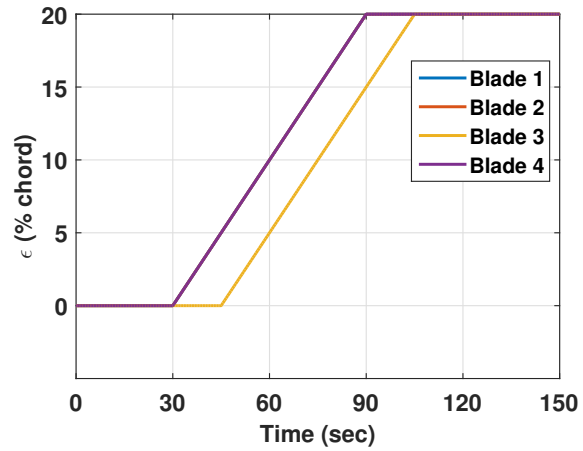

(a) TEP Extension

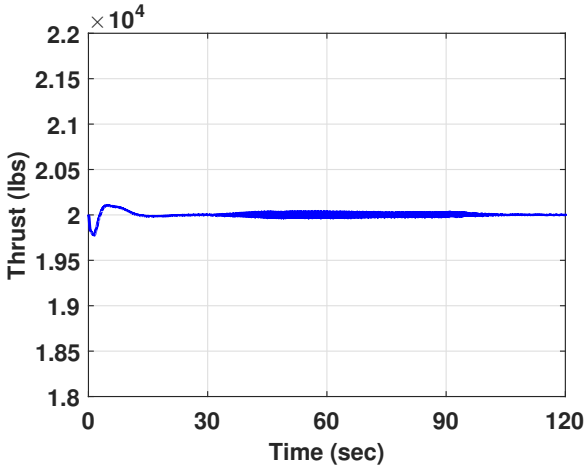

(b) Aircraft Thrust

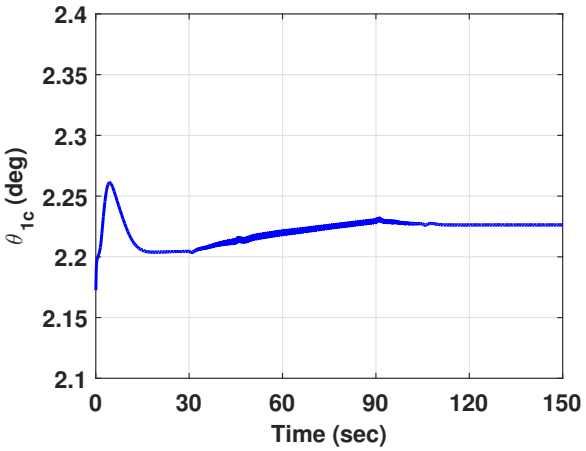

(c) Lateral Cyclic Pitch

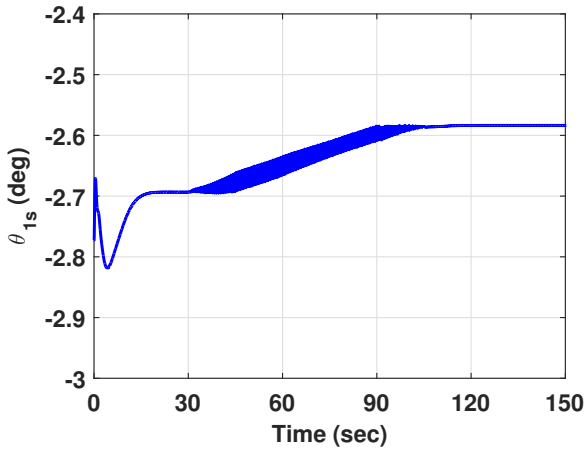

(d) Longitudinal Cyclic Pitch

Fig. 19: Asynchronous chord morphing - 40 knots, sea-level